

Fabrication of Black In₂O₃ with Dense Oxygen Vacancy through Dual Functional Carbon Doping for Enhancing Photothermal CO₂ Hydrogenation

Yuhang Qi

Tianjin University

Jiawei Jiang

Tianjin University

Xichen Liang

University of California

Shuxin Ouyang (✉ oysx@mail.ccnu.edu.cn)

Central China Normal University <https://orcid.org/0000-0002-7650-1245>

Wenbo Mi

Tianjin University <https://orcid.org/0000-0002-9108-9930>

Shangbo Ning

Tianjin University

Lei Zhao

University of California

Jinhua Ye

National Institute for Materials Science <https://orcid.org/0000-0002-8105-8903>

Article

Keywords: indium oxide, carbon doping, oxygen vacancy, photothermal catalysis, CO₂ reduction

Posted Date: November 9th, 2020

DOI: <https://doi.org/10.21203/rs.3.rs-102590/v1>

License: © ⓘ This work is licensed under a Creative Commons Attribution 4.0 International License. [Read Full License](#)

Abstract

Photothermocatalytic CO₂ reduction as the channel of the energy and environmental issues resolution has captured persistent attention in recent years. In₂O₃ has been prompted to be a potential photothermal catalyst in this sector on account of unique physicochemical properties. However, different from the metal-based photothermal catalyst with the nature of efficient light-to-thermal conversion and H₂ dissociation, the wide-bandgap semiconductor needs to be modified to possess wide-wavelength-range absorption and the active surface. It remains a challenge to achieve the two aims simultaneously via single material modulation approach. In this study, one strategy of carbon doping can empower In₂O₃ with two advantageous modifications. The carbon doping can reduce the formation energy of oxygen vacancy, which induces the generation of oxygen-vacancy-rich material. The introduction of oxygen defect levels and carbon doping levels in band gap of In₂O₃ significantly reduces this band gap, which endows it full-spectral and intensive solar light absorption. Therefore, the carbon doped In₂O₃ achieves effective light-to-thermal conversion and delivers a 123.6 mmol g⁻¹ h⁻¹ of CO generation rate with near-unity selectivity, as well as prominent stability in photothermocatalytic CO₂ reduction.

Introduction

Energy shortage could be alleviated by fuel regeneration rely on advanced technology rather than exploitation of existing sources¹⁻³. Compared with the amount of emitted solar energy in one day, fossil fuel outputs seem negligible^{4,5}. Mitigating the unbalanced supply and demand, photothermocatalytic technology has been proposed as a reasonable attempt⁶⁻⁹. On the other hand, CO₂ as a well-known excess substance trapped in the atmosphere, could be converted into the value-added product in both greenhouse gas reduction and synthetic chemical generation¹⁰⁻¹². Typically, high purity CO from CO₂ hydrogenation via reverse water gas shift (RWGS) reaction could be used as raw material for the Fischer-Tropsch synthesis¹³, producing carbonyl-containing compounds¹⁴, acetamides¹⁵, triflate electrophiles¹⁶, and purifying nickel in Mond process¹⁷. In this way, photothermal catalytic CO₂ reduction technology can significantly reduce energy consumption and seems promising for carbon recycle, but the fabrication of high-quality catalyst is not yet mature.

Single-phase In₂O₃ is an impactful thermochemistry catalyst with high selectivity of CO, but its wide-bandgap feature (3.2 eV) leads to unfavorable traits to light absorption (it appears pale-yellow color) and photothermal transformation^{18,19}, which limits its application for photothermal catalysis. To extend the limited optical adsorption, researchers make efforts on pretreated In₂O₃²⁰, such as precious metals loading²¹ and nanostructure coating²². But the catalytic activity of photothermal CO₂ reduction remains low. On the other hand, oxygen vacancy as the active site in In₂O₃ plays important role in CO₂ reduction reaction, it can powerfully adsorb the CO₂ molecules. The unsaturated indium atoms around the oxygen vacancy can gradually dissociate hydrogen inputs to accelerate intermediates formation, then to the products^{23,24}. Therefore, to obtain a higher concentration of oxygen vacancy per unit In₂O₃, nanostructures with high specific surface area seem a promising approach²⁵⁻²⁷. Recently, we reported a novel strategy to fabricate ultrathin 2D black In₂O_{3-x} nanosheet with full spectrum absorption by photo-induced defect engineering. It exhibits a maximum yield rate of 103.2 mmol g_{cat}⁻¹ h⁻¹ and near-unity selectivity for CO generation²⁸. While the oxygen vacancy-rich materials still face the key issue of deactivation due to the refilling of oxygen vacancy during the catalysis process^{29,30}. Therefore, how to prepare catalysts of ordinary nano- and micro- particles with comprehensive advantages including superior photothermal conversion efficiency, high concentration of active sites, and long-term stability is still in exploration.

In this work, we report that a dual functional doping of carbon in In₂O₃ through cost-effective hydrothermal synthesis for highly effective photothermal CO₂ reduction (Scheme 1a). Experimental data and simulation calculations have consistently confirmed that doped carbon works as an interstitial atom inserted in the lattice, which results in both the bandgap reduction to extend light absorption to the full spectrum and the formation of high-concentration and stable oxygen vacancies (Scheme 1b). The wide-wavelength and intensive light absorption facilitate the effective photothermal conversion (400 °C of temperature rising in 10 mins under irradiation of 300 W Xe lamp). Besides, the decrease of formation energy of oxygen vacancy (V_o) due to the carbon

doping enhances the concentration of active sites. The optimized C-In₂O_{3-x} catalyst delivers a CO yield rate of 123.6 mmol g_{cat}⁻¹ h⁻¹ (Table S1) and the remarkable stability with no attenuation even after 20 cycles (one hour per cycle). Therefore, manipulation of doped carbon atoms becomes an internal adjustment strategy in inducing oxygen vacancies and then modulating electron structure and surface property in the In₂O₃ system so as to be suitable for photothermal CO₂ reduction.

Results

Fabrication and characterization of carbon doped In₂O₃

In this experiment, glucose as the carbon source was introduced to prepare carbon doping In(OH)₃ (C-In(OH)₃) nanoparticle precursors (Figure S1 and S2) by hydrothermal reactions. After calcinating in the Ar atmosphere, the C-In(OH)₃ was dehydrated to form C-In₂O_{3-x}, and the morphology remained almost unchanged. Particle size ranged from 50 to 200 nm and the particle surface was covered many small protuberances (Figure 1a) with uniformly distributed carbon (Figure S3). The 0.177 nm spacing on the high-resolution transmission electron microscope (HR-TEM) image confirmed the (440) lattice plane in the cubic In₂O₃ crystalline phase corresponding to Fast Fourier transform (FFT) patterns with diffraction along the [110] axis (Figure 1b). The crystal structure was characterized by powder X-ray diffraction (XRD); all the peaks can be indexed into the standard In₂O₃ PDF card (JCPDS card No.71-2194) (Figure 1c).

In order to investigate the existential form of doped carbon and the relevant structural adjustment in In₂O₃, we simulated the most likely four modalities, including carbon atom substitution for oxygen atom (C_s-O), carbon atom substitution for indium atom at two different positions (C_s-In_a and C_s-In_b), and the interstitial carbon into the lattice of In₂O₃ (C_i). Specific properties, formation energies, bond lengths and ionic valence, were listed in Table S2. The results revealed the interstitial carbon model had the smallest formation energy of 7.59 eV (Figure 1d) and required minimal energy injection than the other three cases. In comparison, model III, the substitution of indium at position B, had the second lowest formation energy. However, the atomic radii of carbon and indium atoms were too far apart for substitution doping to occur³¹. Therefore, we speculated the carbon atom tended to be an interstitial state to anchor into the In₂O₃ lattice. Interstitial carbon could further affect the coordination of neighboring atoms to manipulate electronic properties. As seen from the X-ray absorption fine structure (XAFS), the In K-edge k²χ(k) vibrational lines presented a great difference between C-In₂O_{3-x} and standard cubic In₂O₃, which qualitatively revealed distinct local atomic arrangements (inset of Figure 1e). In Figure 1e, the four main peaks could be regarded as In-In shell and In-O shell in the R space for refined local atomic arrangements. We found that doped carbon atoms shortened the length of In-In bonds and enlarged the length of In-O bonds (Table S3). In addition, the maximum K-edge absorption of C-In₂O₃ was reduced to 27938.7 eV (Figure S4), indicating the generation of oxygen vacancy, the coordination number reduction of In-O and In-In, which resulted in higher disorder degrees^{32,33}. Compared with standard cubic In₂O₃, the C-In₂O₃ with the presence of a noticeable structure distortion helped to maintain structural stability^{34,35}.

Raman spectra provided more proof on local structural change and distortion of C-In₂O_{3-x} (Figure S5). Distinct photon modes at 309, 407, 491, and 628 cm⁻¹ were consistent with Raman active modes of the cubic structure In₂O₃^{36,37}, but when the carbon was doped into the In₂O₃ lattice with different carbon doping levels, these highlighted peaks become smoother, suggesting introduced carbon disrupts original lattice structure³⁸. To investigate the effect of doped carbon on the chemical state and electronic structure of In₂O₃, we performed X-ray photoelectron spectroscopy (XPS) characterization. From the In 3d core-level spectra (Figure 1f), the two peaks located at 443.7 eV and 451.4 eV were assigned to the In 3d_{5/2} and In 3d_{3/2} signals^{39,40}. However, with interference from carbon, both peaks moved toward higher binding energy with an about 0.5 eV shift, confirming indium atoms did accept electrons from doped carbon. To prove the XPS results, we computed the charge difference density (isosurface value is 3 e nm⁻³) of model IV in Figure 1d and found much net gain of charge was distributed around indium atom (inset of Figure 1f). Experimental data corroborated theoretical calculation, proving that carbon was successfully anchored in the lattice of In₂O₃ and therefore altered its original electronic structure.

Photothermal CO₂ reduction performance

To reveal the advantages of C-In₂O₃ in the photothermal-driven RWGS reaction, we conducted the catalytic performance tests (Figure 2a) of the V_o-poor In₂O₃, V_o-rich In₂O_{3-x} and C-In₂O_{3-x} with different carbon doping levels (Table S4). Benefiting from the richer concentration of active sites, V_o-rich In₂O_{3-x} had 18.2 mmol g_{cat}⁻¹ h⁻¹ of CO production rate, which was three times higher than that of V_o-poor In₂O₃. This result was consistent with the literature analyses that oxygen vacancy facilitated CO₂ adsorption to yield high RWGS reactivity^{18,23,41}. When the appropriate amount of carbon was doped, the catalytic activity of C-In₂O_{3-x} achieved six-fold enlargement compared with V_o-rich In₂O_{3-x} (123.6 mmol g_{cat}⁻¹ h⁻¹). Low doping concentration limited light absorption capacity to enhance the photothermal conversion efficiency in endothermic RWGS reaction while high doping concentration led that extra carbon cannot anchor in the In₂O₃ lattice and form inert "free carbon" around the In₂O₃ nanoparticle to compete for the light energy. The more detail of the mechanism for the high activity will be discussed in next section. With the optimal sample, the CO₂ conversion rate of C-In₂O_{3-x} eventually reached 45% with near-unity CO selectivity without the production of CH₄ (Figure 2b) and the remarkable catalytic performance kept holding beyond 20 cycles in stability test (Figure 2c). The blank control test under the photothermal conditions also confirmed the doped carbon in the C-In₂O_{3-x} was stable and could not be decomposed to CO₂ or CO (Figure S6). Further, the turnover number of the cyclic stability test (the amount of yield product/the amount of catalyst) was 190.56 that was much larger than 1, indicating photothermal RWGS reaction exhibits typical feature of catalysis.

Mechanism and pathway of photothermal CO₂ reduction

Photothermal catalysis of CO₂ reduction involves two main steps. The first step is light absorption and photothermal transformation via the active sites on the catalyst surface (local temperature effect); the second is CO₂ adsorption and subsequent catalytic process²⁸. In the first step, the catalysts are required to possess broader spectral coverage to maximize energy absorption and energy transfer efficiency. Because the photoexcited carriers (electron-hole pairs) could heat the non-plasmonic C-In₂O_{3-x} through non-radiative recombination from either Auger or Shockley-Read-Hall (i.e., trap assisted) to drive the thermally catalytic process, which rendered the mechanism for lattice vibrations and heat generation^{6,42}, and powerfully assisted in lowering the photochemical activation energy^{43,44}. Unlike the pale yellow of In₂O₃ crystals or the pale gray of In₂O_{3-x}, the color of C-In₂O_{3-x} appeared jet black (inset of Figure 3a), having broader photon absorption ranges from 250 to 2400 nm and stronger absorption intensity. Doped carbon atoms could extend the scope to the visible light region and defect state caused by oxygen vacancy further extended it to infrared region (Figure 3a). Combined with the bandgap structure (Figure S7) and ultraviolet photoelectron spectroscopy (UPS) (Figure S8), a schematic illustration of the bandgap structure of C-In₂O_{3-x} was depicted and shown in Figure S9. The band structure and density of states (DOS) of C-In₂O_{3-x} regulated by doped carbon could be explained using density functional theory (DFT). In Figure S10, compared with the cubic In₂O₃, when an oxygen vacancy was generated around an interstitial carbon, a new defect energy level with more massive DOS emerges. In this case, the electrons can be easily excited into the conduction band through the intermediate state, thereby achieving higher photoconversion efficiency⁴⁵⁻⁴⁷.

On the other hand, the radiative recombination competed against non-radiative recombination. After carbon doping, the fluorescence significantly quenched, demonstrating that radiative recombination of the photon-generated carriers had been suppressed by extracting the electrons (Figure S11). Therefore, the C-In₂O_{3-x} system could reach near 400 °C within 10 minutes, which is far higher temperature than those of V_o-poor In₂O₃ and V_o-rich In₂O_{3-x} (Figure 3b). The surface of C-In₂O_{3-x} worked as a "nanoscale heat source," which absorbed the photon energy and rapidly converted it into heat that was conducted to the active sites of C-In₂O_{3-x} in a short time.

The next step was adsorption of gas molecules onto the surface and subsequent catalytic process. For clarity, in temperature-programmed desorption (TPD) of CO₂, the peak at 480°C indicated the adsorption was in the form of chemisorption via the oxygen vacancies on C-In₂O_{3-x}^{48,49}. If the oxygen vacancy is filled under annealing in air, the adsorption capacity could be notably reduced (Figure S12). In order to prove the role of oxygen vacancy as the active site was in the catalytic process, we conducted comparative DFT calculations of In₂O₃ and In₂O₃-O_{vac} [110] slabs (Figure S13 -15). The Gibbs free energy for the intermediate *CO of RWGS reaction on In₂O₃ slab without oxygen vacancy was 0.66 eV which was higher than the slab with oxygen vacancy (0.32 eV). Thus, a high concentration of oxygen vacancies was expected to increase the capacity of CO₂ adsorption and lower the energy barrier of photothermal CO₂ reduction RWGS reaction. Electron spin resonance spectroscopy (ESR) effectively evaluated the oxygen vacancy concentration (Figure 3c). Limited signals of V_o-poor In₂O₃ and V_o-rich In₂O_{3-x} were detected, while a stronger signal of C-In₂O_{3-x} appeared at g=2.004, which could be explained as more concentrated electrons are trapped around the surface oxygen vacancies⁵⁰. Next, to prove the carbon doping has a function in elevating oxygen vacancy concentration, the formation energy of oxygen vacancy was simulated (inset of Figure 3c). In non-defective In₂O₃ crystal, the oxygen vacancy formation energy was 4.98 eV, while the energy decreased to 3.10 eV after interstitial carbon anchored into In₂O₃ lattice (Table S3). Our result suggested that interstitial carbon assembled with oxygen vacancy to form a higher concentration active sites, thereby pushing forward the RWGS reaction.

We then performed the in-situ Fourier Transform Infrared (FTIR) characterization in a flow cell to investigate the catalytic pathway of RWGS reaction on the active sites of C-In₂O_{3-x}. As displayed in Figure 3d, the C-In₂O_{3-x} exhibited OH stretching band within the range 3400-3730 cm⁻¹. Peaks located at 1500 and 1390 cm⁻¹ were identified as chemisorbed CO₂ and H₂ molecules, as well as bicarbonate (HCO₃⁻) and carbonate (CO₃⁻) formation. The detectable peak at 2894 cm⁻¹ was attributed to bending vibration δ(CH). Here, the peaks corresponding to crucial intermediate methoxy (H₃CO*) in the spectra were at 2839 and 1090 cm⁻¹, and COOH* were at 1578 and 1232 cm⁻¹. Therefore, the incoming electrons coupled with resident protons reduced the amount of CO₂ molecules at the active sites, oxygen vacancy, then formed COOH* and H₃CO* intermediates and transferred into CO* consistently. Simultaneously, the peak at 2107 cm⁻¹ and 1643 cm⁻¹ were the diagnostic vibrational modes of CO and H₂O respectively, indicating the reaction pathway that features CO* as the intermediate from carboxyl through the RWGS reaction⁵¹⁻⁵⁴. In general, oxygen vacancy with doped carbon as active sites effectively activated CO₂ molecules and stabilized the intermediates, so as to reduce the activation energy and promote photothermal CO₂ reduction (Figure 3e).

Discussion

In summary, photothermal catalytic CO₂ reduction is a promising technology to alter the traditional thermo-catalytic reaction, which thermodynamically improves activity under light conditions without additional energy input. The dual-function carbon doping is a feasible option to enhance and stabilize photothermal catalyst activity of In₂O₃. Doped carbon is more conducive to the light absorption and the photothermal conversion efficiency improvement; benefiting from formation energy reduction of oxygen vacancy, high concentration active sites are obtainable. As a result, the C-In₂O_{3-x} has 123.6 mmol g⁻¹ h⁻¹ of CO production rates and nearly 100% selectivity. This work demonstrates that the microstructure modulation of crystal defect in catalyst can significantly enhanced the utilization of solar light and then to drive efficient and stable catalytic reaction, which achieves high-performance solar-to-chemical energy conversion.

Experimental Section

Materials: Synthesis of V_o-poor In₂O₃ and V_o-rich In₂O_{3-x} nano particles: First, 1 mmol indium nitrate was added into 60 mL deionized water, magnetically stirred for 20 min, then mixed with 3 mmol urea followed by another 10 min stirring. After, the mixture was transferred into a 100 mL Teflon-lined stainless-steel autoclave, sealed and maintained at 140°C for 12 hours. The whole system naturally cools down to room temperature. After centrifuging the mixture, the final product was collected, washed with distilled water and ethanol several times and then dried in air at 60°C. Calcination is at 600 °C for 2 h in air and H₂-Ar with a heating rate of 5 °C min⁻¹ to fabricate the V_o-poor In₂O₃ and V_o-rich In₂O_{3-x}. The synthesis procedure for C-In₂O₃ is similar to that

of V_o-poor In₂O₃ and V_o-rich In₂O_{3-x}, except that 1 mmol of indium nitrate, 3 mmol urea and different amounts of glucose (0.1, 0.2, 0.3, 0.4, and 0.5 g) were simultaneously added into the starting solution for hydrothermal synthesis, and calcination at 600 °C for 2 h in Ar.

Reaction condition and activity evaluation: Photothermal CO₂ conversion by H₂ was carried out in a batch type reaction system with a total volume of 330 ml. After evacuation of reaction system, CO₂ and H₂ (the molar ratio of H₂ to CO₂ is 1:1) were injected. A 300W Xe lamp was used as irradiation source to drive the photothermal CO₂ conversion. The light intensity is 2.98 W cm⁻². The temperature of catalyst surface is measured by the infrared thermometer, and the reflectance coefficient is 0.78. For all experiments, 0.05 g of sample was used and spread onto a round shape air-permeable quartz fiber filter with the area of 7 cm². The quartz fiber filter film is fixed on the stage inside the reactor. The tip of thermometer was maintained an intimate contact with the sample (thickness of catalyst powder is about 1~2 mm). The contents of CO₂ and CO in the reaction system were sampled and measured with a gas chromatograph (GC-2014, Shimadzu) equipped with a methanizer and flame ionization detector according to the standard curves.

Sample characterization: XRD patterns were recorded on an X-Pert diffractometer equipped with graphite monochromatized Cu-K radiation. The morphologies were characterized by field-emission SEM (Hitachi, s4800) and TEM (JEOL, 2100F). The diffuse reflection spectra of catalysts were measured by UV-vis-NIR spectrophotometer (Shimadzu, UV-3600) from 220 to 2400 nm. Chemical valence of the surface was analyzed by XPS (Escalab 250Xi, Thermo Scientific, America). The PL properties of materials were investigated by PL spectra (Horiba Fluorolog-3) with the excitation light wavelength of 350 nm. The ESR spectra measurements were executed on JES-FA200 X-band spectrometer. The catalyst temperature was probed by a digital thermometer (Custom, CT-1200D). Raman spectra were recorded by Horiba (Xplora Plus) instrument. The pore size distribution was determined with a surface area analyzer (BEL Sorp-II mini, BEL Japan Co., Japan) by the BET method. The FTIR spectrum was executed on Nicolet 6700. In situ FTIR spectra have been recorded by a Nicolet 6700 Fourier transform instrument, using conventional IR cells connected to a gas manipulation apparatus. XAS measurement for the In K-edge was performed in fluorescence mode on beamline 20-BM-B with electron energy of 7 GeV and an average current of 100 mA which is located in the Advanced Photon Source at Argonne National Laboratory.

Declarations

Acknowledgements

This work received financial support from the National Natural Science Foundation of China (Grants 21972052 and 21633004) and JSPS KAKENHI of Japan (Grant Number JP18H02065).

References

1. Walter, M.G. et al. Solar Water Splitting Cells. *Chem Rev* **110**, 6446-6473 (2010).
2. Chu, S. & Majumdar, A. Opportunities and challenges for a sustainable energy future. *Nature* **488**, 294-303 (2012).
3. Dusastre, V. & Martiradonna, L. Materials for sustainable energy. *Nat Mater* **16**, 15-15 (2017).
4. Brockway, P.E., Owen, A., Brand-Correa, L.I. & Hardt, L. Estimation of global final-stage energy-return-on-investment for fossil fuels with comparison to renewable energy sources. *Nature Energy* **4**, 612-621 (2019).
5. Shindell, D. & Smith, C.J. Climate and air-quality benefits of a realistic phase-out of fossil fuels. *Nature* **573**, 408-411 (2019).
6. Ghoussoub, M., Xia, M., Duchesne, P.N., Segal, D. & Ozin, G. Principles of photothermal gas-phase heterogeneous CO₂ catalysis. *Energ Environ Sci* **12**, 1122-1142 (2019).
7. Li, Z.H. et al. Co-Based Catalysts Derived from Layered-Double-Hydroxide Nanosheets for the Photothermal Production of Light Olefins. *Adv Mater* **30**, 1800527 (2018).

8. Ren, J. et al. Targeting Activation of CO₂ and H₂ over Ru-Loaded Ultrathin Layered Double Hydroxides to Achieve Efficient Photothermal CO₂ Methanation in Flow-Type System. *Adv Energy Mater* **7**, 1601657 (2017).
9. Zhao, L. et al. Solar-Driven Water-Gas Shift Reaction over CuO_x/Al₂O₃ with 1.1 % of Light-to-Energy Storage. *Angew Chem Int Ed Engl* **58**, 7708-7712 (2019).
10. Hoegh-Guldberg, O. et al. The human imperative of stabilizing global climate change at 1.5 degrees C. *Science* **365**, 1263 (2019).
11. Liu, C., Colon, B.C., Ziesack, M., Silver, P.A. & Nocera, D.G. Water splitting-biosynthetic system with CO₂ reduction efficiencies exceeding photosynthesis. *Science* **352**, 1210-1213 (2016).
12. Asadi, M. et al. Nanostructured transition metal dichalcogenide electrocatalysts for CO₂ reduction in ionic liquid. *Science* **353**, 467-470 (2016).
13. Ellis, P.R., Enache, D.I., James, D.W., Jones, D.S. & Kelly, G.J. A robust and precious metal-free high performance cobalt Fischer–Tropsch catalyst. *Nat Catal* **2**, 623-631 (2019).
14. Zhu, C., Liu, J., Li, M.B. & Backvall, J.E. Palladium-catalyzed oxidative dehydrogenative carbonylation reactions using carbon monoxide and mechanistic overviews. *Chem Soc Rev* **49**, 341-353 (2019).
15. Jouny, M. et al. Formation of carbon-nitrogen bonds in carbon monoxide electrolysis. *Nat Chem* **11**, 846-851 (2019).
16. Kinney, R.G. & Arndtsen, B.A. Decarboxylation with Carbon Monoxide: The Direct Conversion of Carboxylic Acids into Potent Acid Triflate Electrophiles. *Angew Chem Int Ed Engl* **58**, 5085-5089 (2019).
17. Morris, P.J.T. The Legacy of Mond, Ludwig. *Endeavour* **13**, 34-40 (1989).
18. Hou, J. et al. Atomically Thin Mesoporous In₂O_{3-x}/In₂S₃ Lateral Heterostructures Enabling Robust Broadband-Light Photo-Electrochemical Water Splitting. *Adv Energy Mater* **8**, 1701114 (2018).
19. Chao, Y. et al. Ultrathin Visible-Light-Driven Mo Incorporating In₂O₃-ZnIn₂Se₄ Z-Scheme Nanosheet Photocatalysts. *Adv Mater* **31**, e1807226 (2019).
20. Wang, L. et al. Black indium oxide a photothermal CO₂ hydrogenation catalyst. *Nat Commun* **11** (2020).
21. Rui, N. et al. CO₂ hydrogenation to methanol over Pd/In₂O₃: effects of Pd and oxygen vacancy. *Applied Catalysis B: Environmental* **218**, 488-497 (2017).
22. Hoch, L.B. et al. Nanostructured Indium Oxide Coated Silicon Nanowire Arrays: A Hybrid Photothermal/Photochemical Approach to Solar Fuels. *Acs Nano* **10**, 9017-9025 (2016).
23. Ye, J., Liu, C., Mei, D. & Ge, Q. Active Oxygen Vacancy Site for Methanol Synthesis from CO₂ Hydrogenation on In₂O₃(110): A DFT Study. *Acs Catal* **3**, 1296-1306 (2013).
24. Gao, P. et al. Direct conversion of CO₂ into liquid fuels with high selectivity over a bifunctional catalyst. *Nat Chem* **9**, 1019-1024 (2017).
25. Ha, M. et al. Multicomponent Plasmonic Nanoparticles: From Heterostructured Nanoparticles to Colloidal Composite Nanostructures. *Chem Rev* **119**, 12208-12278 (2019).
26. Prieto, G. et al. Hollow Nano- and Microstructures as Catalysts. *Chem Rev* **116**, 14056-14119 (2016).
27. Cao, X., Tan, C., Sindoro, M. & Zhang, H. Hybrid micro-/nano-structures derived from metal-organic frameworks: preparation and applications in energy storage and conversion. *Chem Soc Rev* **46**, 2660-2677 (2017).
28. Qi, Y. et al. Photoinduced Defect Engineering: Enhanced Photothermal Catalytic Performance of 2D Black In₂O_{3-x} Nanosheets with Bifunctional Oxygen Vacancies. *Adv Mater* **32**, 1903915 (2019).
29. Li, L. et al. Insight into the Effect of Oxygen Vacancy Concentration on the Catalytic Performance of MnO₂. *Acs Catal* **5**, 4825-4832 (2015)..
30. Cui, Y.L.S. et al. Refilling Nitrogen to Oxygen Vacancies in Ultrafine Tungsten Oxide Clusters for Superior Lithium Storage. *Adv Energy Mater* **9**, 1902148 (2019).
31. Yu, W., Zhang, J. & Peng, T. New insight into the enhanced photocatalytic activity of N-, C- and S-doped ZnO photocatalysts. *Applied Catalysis B: Environmental* **181**, 220-227 (2016).

32. Zhao, Y. et al. Defect-Rich Ultrathin ZnAl-Layered Double Hydroxide Nanosheets for Efficient Photoreduction of CO₂ to CO with Water. *Adv Mater* **27**, 7824-7831 (2015).
33. Haneda, M., Kintaichi, Y., Bion, N. & Hamada, H. Mechanistic study of the effect of coexisting H₂O on the selective reduction of NO with propene over sol-gel prepared In₂O₃-Al₂O₃ catalyst. *Applied Catalysis B: Environmental* **42**, 57-68 (2003).
34. Sun, Y., Gao, S., Lei, F. & Xie, Y. Atomically-thin two-dimensional sheets for understanding active sites in catalysis. *Chem Soc Rev* **44**, 623-636 (2015).
35. Sun, Y. et al. Fabrication of flexible and freestanding zinc chalcogenide single layers. *Nat Commun* **3**, 1057 (2012).
36. Kranert, C., Schmidt-Grund, R. & Grundmann, M. Raman active phonon modes of cubic In₂O₃. *physica status solidi (RRL) - Rapid Research Letters* **8**, 554-559 (2014).
37. Yin, W.Y. et al. In(OH)₃ and In₂O₃ Micro/Nanostructures: Controllable NaOAc-Assisted Microemulsion Synthesis and Raman Properties. *J Phys Chem C* **113**, 19493-19499 (2009).
38. Gu, F.B., Li, C.J., Han, D.M. & Wang, Z.H. Manipulating the Defect Structure (V-O) of In₂O₃ Nanoparticles for Enhancement of Formaldehyde Detection. *Acs Appl Mater Inter* **10**, 933-942 (2018).
39. Cao, S.-W. et al. Solar-to-fuels conversion over In₂O₃/g-C₃N₄ hybrid photocatalysts. *Applied Catalysis B: Environmental* **147**, 940-946 (2014).
40. Prim, A. et al. A Novel Mesoporous CaO-Loaded In₂O₃ Material for CO₂ Sensing. *Advanced Functional Materials* **17**, 2957-2963 (2007).
41. Ye, J., Liu, C. & Ge, Q. DFT Study of CO₂ Adsorption and Hydrogenation on the In₂O₃ Surface. *The Journal of Physical Chemistry C* **116**, 7817-7825 (2012).
42. Hoch, L.B. et al. Carrier dynamics and the role of surface defects: Designing a photocatalyst for gas-phase CO₂ reduction. *Proc Natl Acad Sci* **113**, 8011-8020 (2016).
43. He, L. et al. Spatial Separation of Charge Carriers in In₂O_{3-x}(OH)_y Nanocrystal Superstructures for Enhanced Gas-Phase Photocatalytic Activity. *Acs Nano* **10**, 5578-5586 (2016).
44. Ghuman, K.K. et al. Illuminating CO₂ reduction on frustrated Lewis pair surfaces: investigating the role of surface hydroxides and oxygen vacancies on nanocrystalline In₂O_{3-x}(OH)_y. *Phys Chem Chem Phys* **17**, 14623-14635 (2015).
45. Yang, M.Q. et al. Disorder Engineering in Monolayer Nanosheets Enabling Photothermic Catalysis for Full Solar Spectrum (250-2500 nm) Harvesting. *Angew Chem Int Edit* **58**, 3077-3081 (2019).
46. Rahman, M.A. et al. Defect-rich decorated TiO₂ nanowires for super-efficient photoelectrochemical water splitting driven by visible light. *Energ Environ Sci* **8**, 3363-3373 (2015).
47. Nowotny, J. et al. Defect chemistry and defect engineering of TiO₂-based semiconductors for solar energy conversion. *Chem Soc Rev* **44**, 8424-8442 (2015).
48. Rui, N. et al. CO₂ hydrogenation to methanol over Pd/In₂O₃: effects of Pd and oxygen vacancy. *Appl Catal B-Environ* **218**, 488-497 (2017).
49. Martin, O. et al. Indium Oxide as a Superior Catalyst for Methanol Synthesis by CO₂ Hydrogenation. *Angew Chem Int Ed Engl* **55**, 6261-6265 (2016).
50. Lei, F. et al. Oxygen Vacancies Confined in Ultrathin Indium Oxide Porous Sheets for Promoted Visible-Light Water Splitting. *J Am Chem Soc* **136**, 6826-6829 (2014).
51. Yan, T. et al. Polymorph selection towards photocatalytic gaseous CO₂ hydrogenation. *Nat Commun* **10**, 1-10 (2019).
52. Chen, G. et al. From Solar Energy to Fuels: Recent Advances in Light-Driven C1 Chemistry. *Angew Chem Int Ed Engl* **58**, 17528-17551 (2019).
53. Sun, Q., Liu, C.W., Pan, W., Zhu, Q.M. & Deng, J.F. In situ IR studies on the mechanism of methanol synthesis over an ultrafine Cu/ZnO/Al₂O₃ catalyst. *Appl Catal a-Gen* **171**, 301-308 (1998).
54. Choi, S. et al. Catalytic behavior of metal catalysts in high-temperature RWGS reaction: In-situ FT-IR experiments and first-principles calculations. *Sci Rep* **7**, 41207 (2017).

Scheme

Scheme 1 is available in the Supplementary Files.

Figures

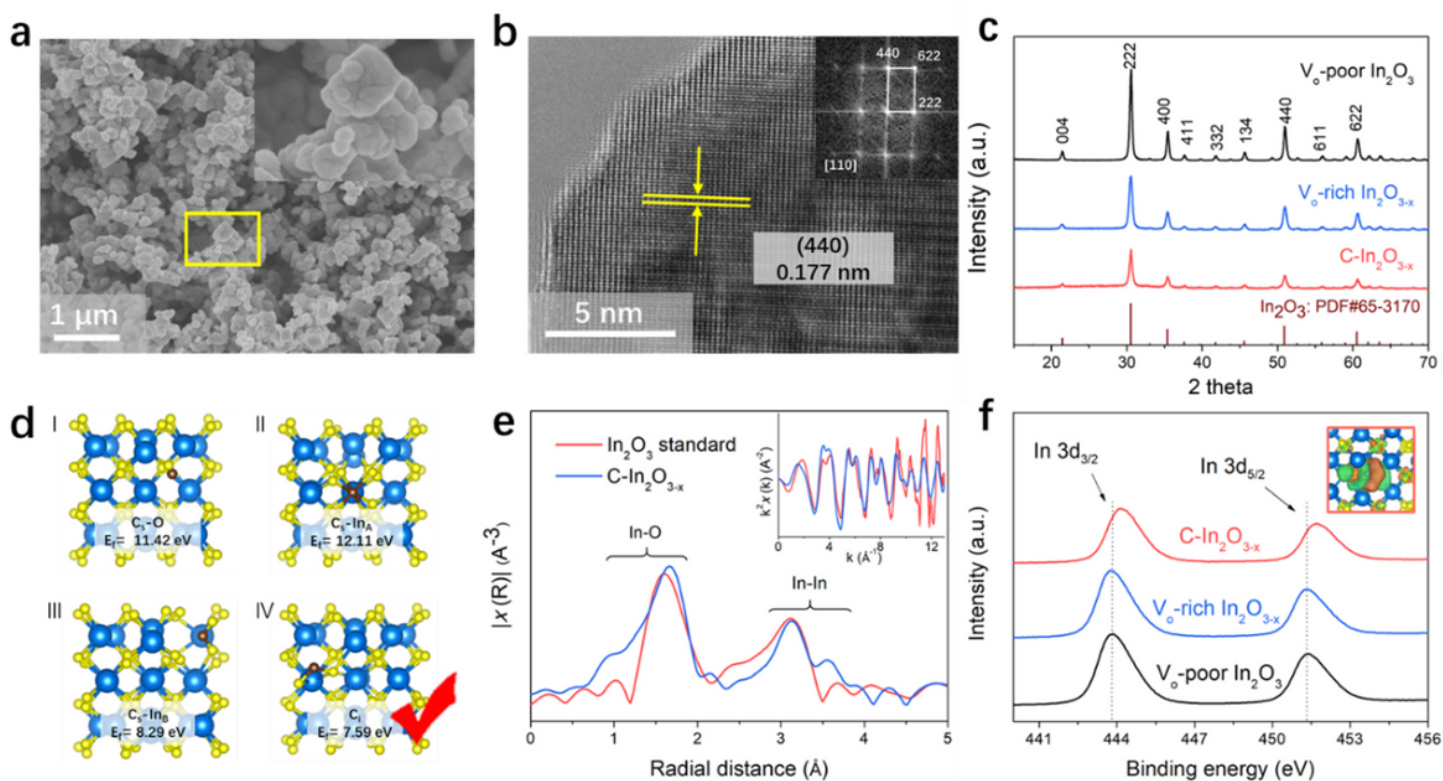


Figure 1

(a) SEM of C-In₂O_{3-x}, inset: the part of the region enclosed by the yellow square, (b) HR-TEM image of C-In₂O_{3-x}, inset: The Fast Fourier transform corresponding yellow square, (c) XRD patterns of Vo-poor In₂O₃, Vo-rich In₂O_{3-x} and C-In₂O_{3-x}, (d) Formation energy of Cs-O, Cs-In_a, Cs-In_b and C_i, (e) In K-edge extended XAFS oscillation function $k^2\chi(k)$, Inset: the corresponding Fourier-transformed data for standard In₂O₃ and C-In₂O_{3-x}, (f) XPS spectra of the In 3d core level peak regions of C-In₂O_{3-x}, inset: charge difference density of In₂O₃ with one C atom interstitial with one O atom vacancy.

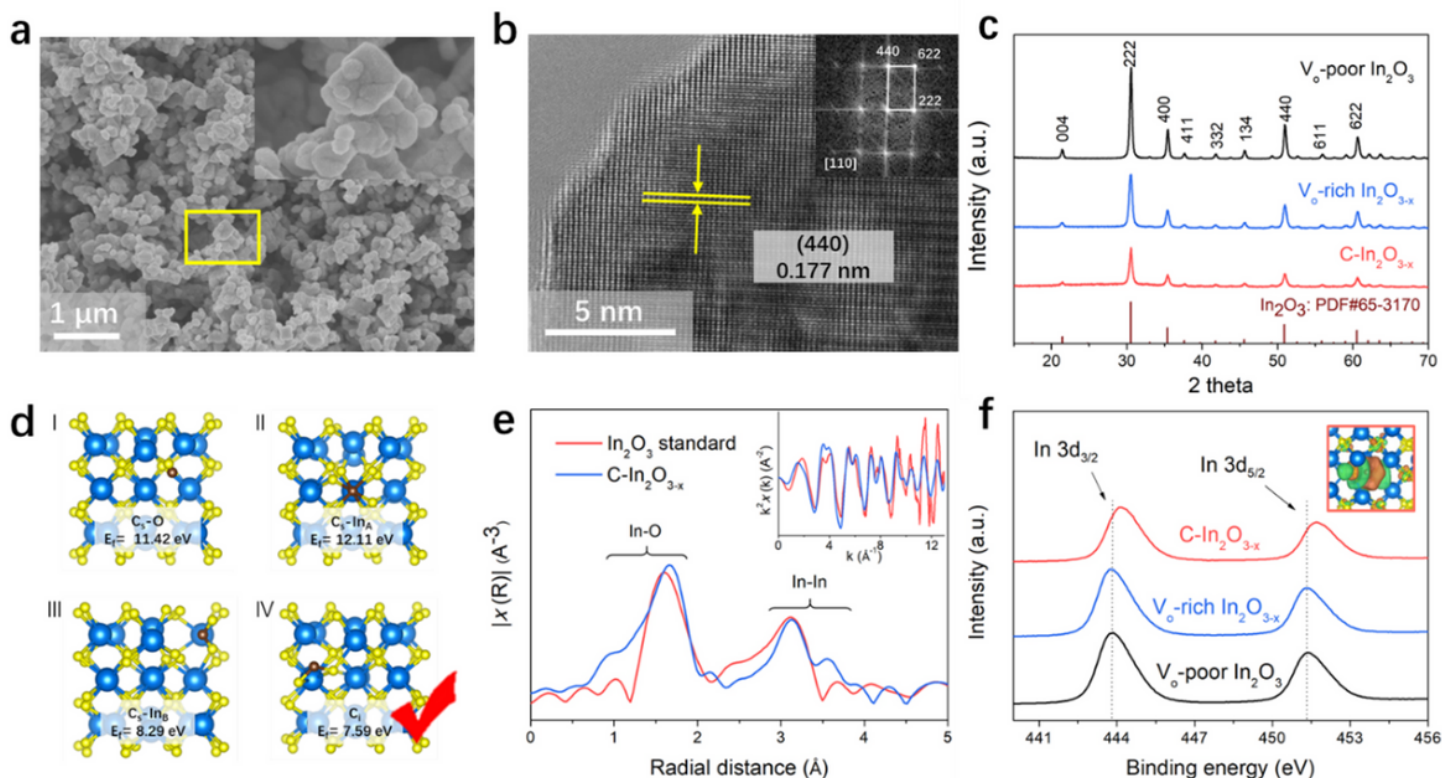


Figure 1

(a) SEM of C-In₂O_{3-x}, inset: the part of the region enclosed by the yellow square, (b) HR-TEM image of C-In₂O_{3-x}, inset: The Fast Fourier transform corresponding yellow square, (c) XRD patterns of V_o-poor In₂O₃, V_o-rich In₂O_{3-x} and C-In₂O_{3-x}, (d) Formation energy of Cs-O, Cs-In_a, Cs-In_b and C_i, (e) In K-edge extended XAFS oscillation function $k^2\chi(k)$, Inset: the corresponding Fourier-transformed data for standard In₂O₃ and C-In₂O_{3-x}, (f) XPS spectra of the In 3d core level peak regions of C-In₂O_{3-x}, inset: charge difference density of In₂O₃ with one C atom interstitial with one O atom vacancy.

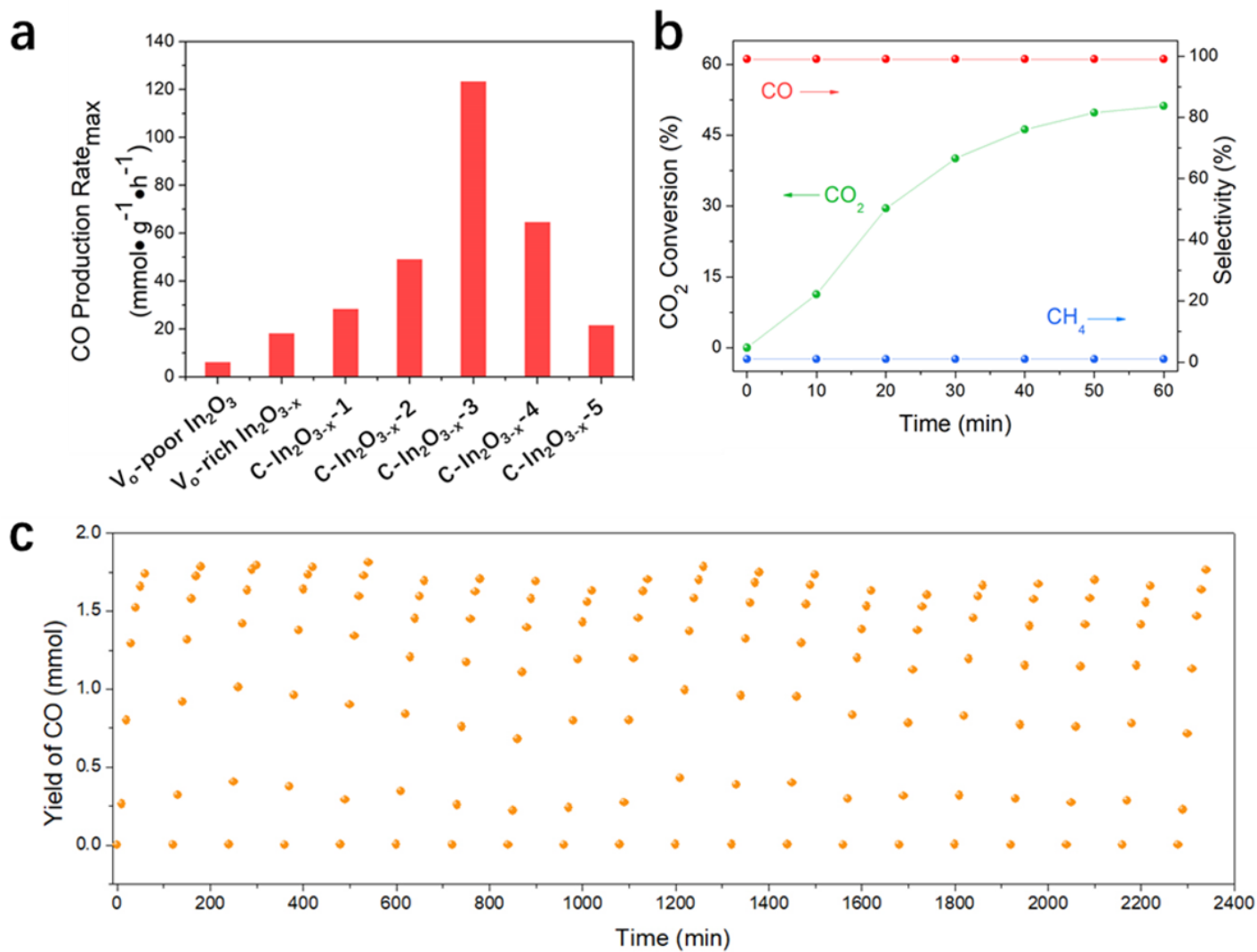


Figure 2

(a) CO production rates of V_o-poor In₂O₃, V_o-rich In₂O_{3-x} and C-In₂O_{3-x} with different carbon content, (b) photothermal CO₂ conversion test and selectivity of C-In₂O_{3-x-3}. Reaction condition: 50 mg catalysts, H₂: CO₂=1:1, 300 W Xenon lamp, (c) Cyclic stability testing of C-In₂O_{3-x-3}.

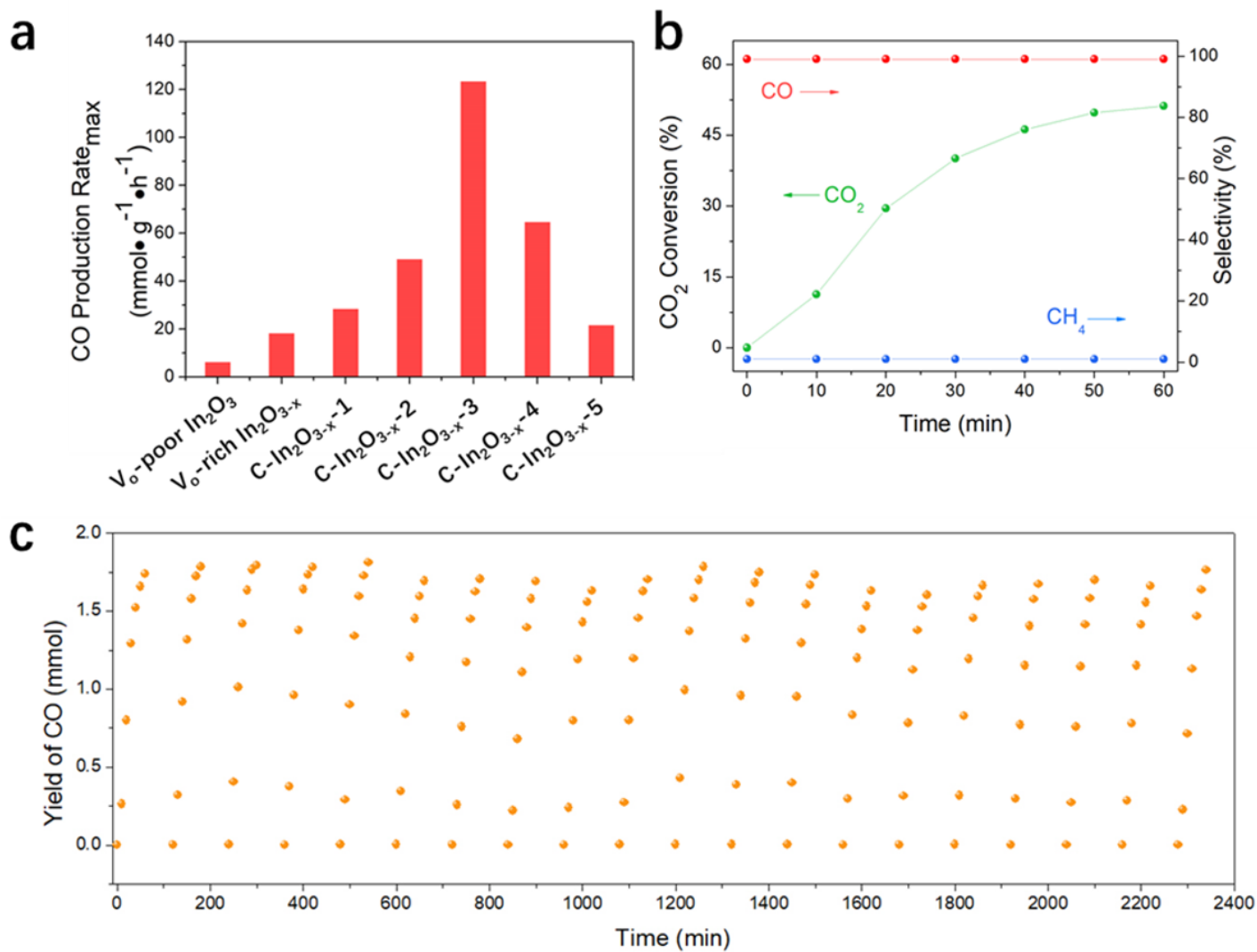


Figure 2

(a) CO production rates of V_o-poor In₂O₃, V_o-rich In₂O_{3-x} and C-In₂O_{3-x} with different carbon content, (b) photothermal CO₂ conversion test and selectivity of C-In₂O_{3-x}-3. Reaction condition: 50 mg catalysts, H₂: CO₂=1:1, 300 W Xenon lamp, (c) Cyclic stability testing of C-In₂O_{3-x}-3.

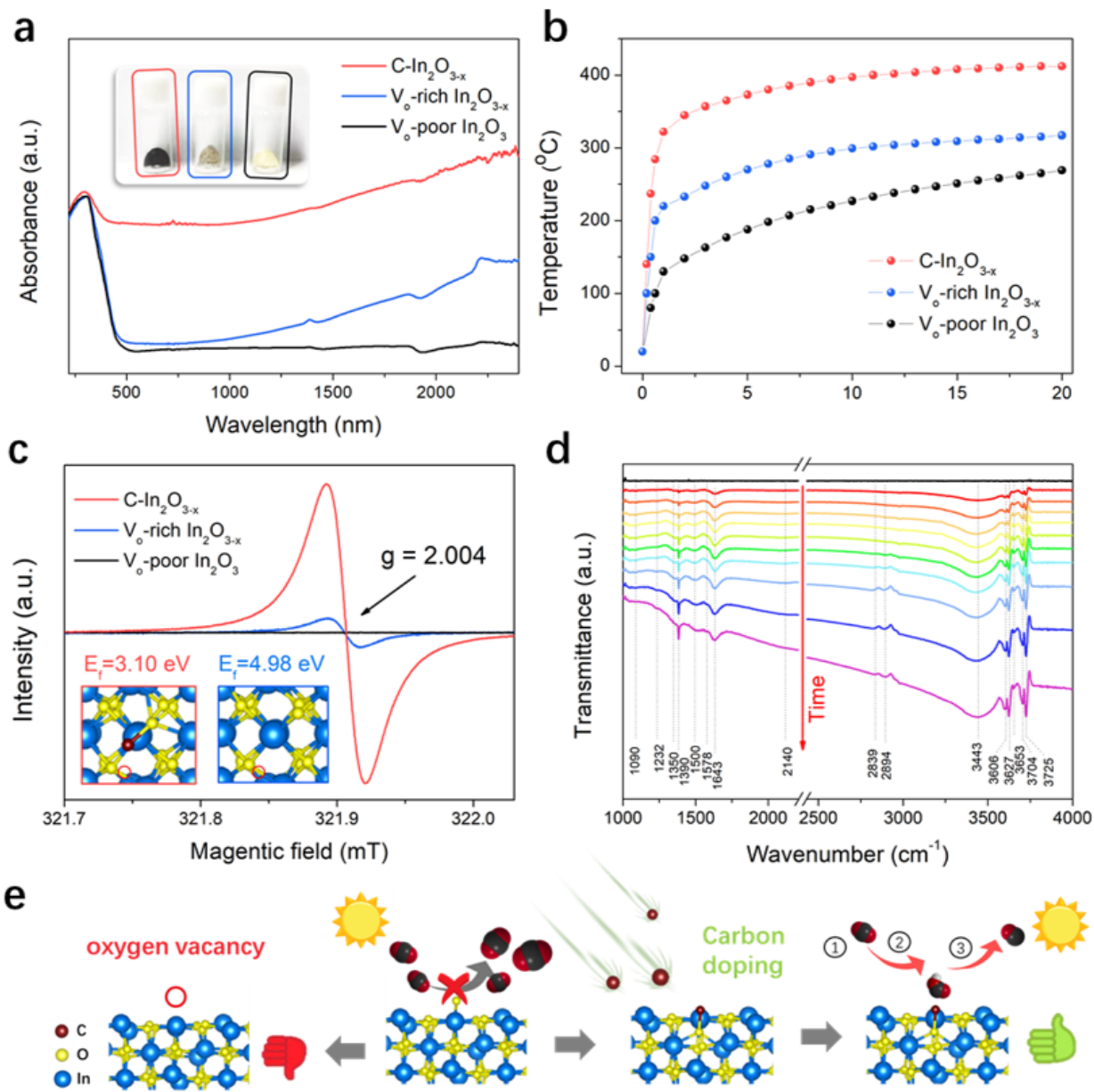


Figure 3

(a) UV- visible -NIR spectra, Inset: digital photo, (b) Temperature monitoring of photothermal conversion of CO₂ system, (c) Electron spin resonance spectra, Inset: Oxygen vacancy formation energy of perfect In₂O₃ and C-In₂O₃, (d) in situ FT-IR spectra, (e) Advantages for CO₂ photothermal reduction into CO over the C-In₂O_{3-x}.

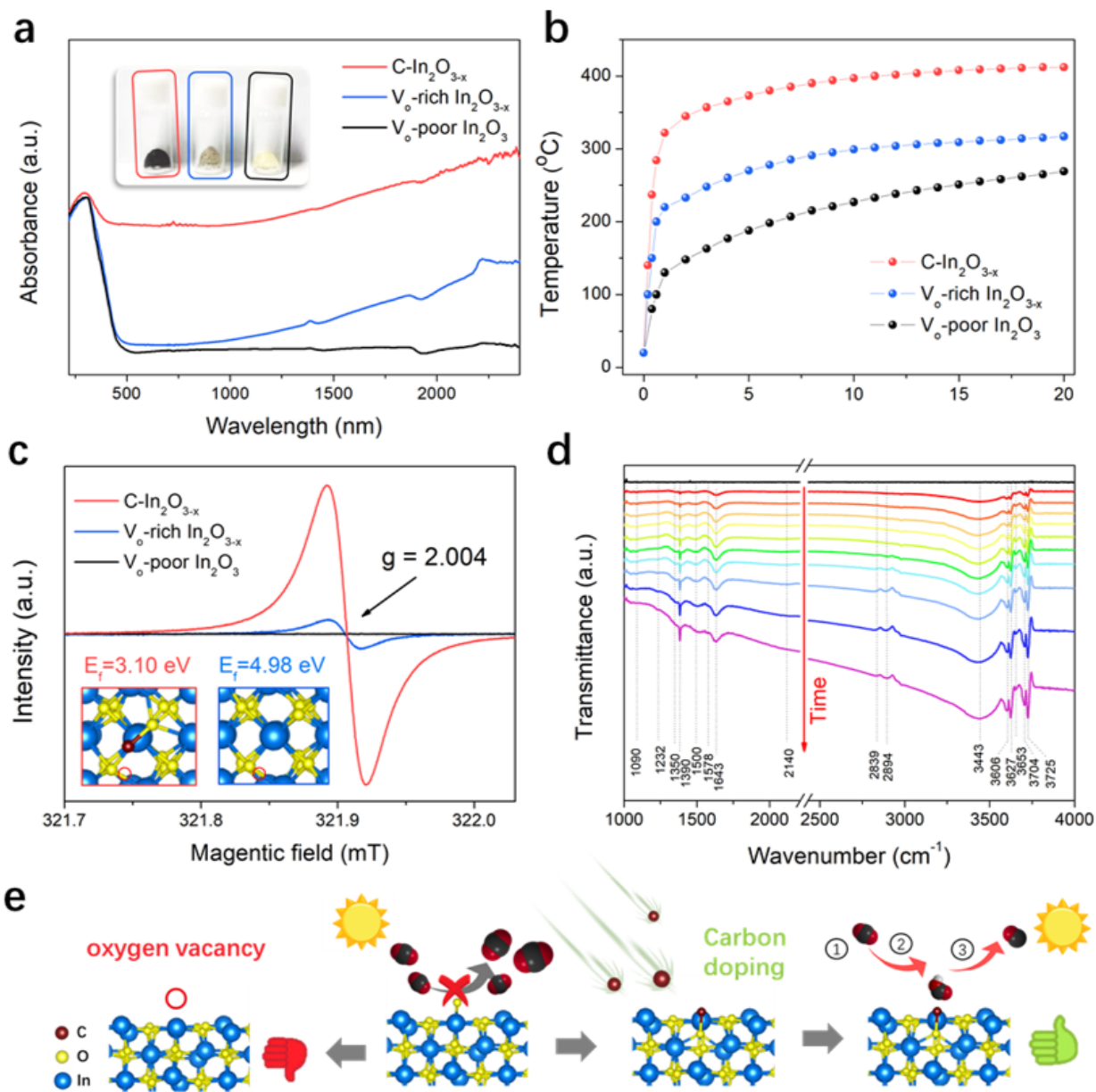


Figure 3

(a) UV- visible -NIR spectra, Inset: digital photo, (b) Temperature monitoring of photothermal conversion of CO₂ system, (c) Electron spin resonance spectra, Inset: Oxygen vacancy formation energy of perfect In₂O₃ and C-In₂O₃, (d) in situ FT-IR spectra, (e) Advantages for CO₂ photothermal reduction into CO over the C-In₂O₃-x.

Supplementary Files

This is a list of supplementary files associated with this preprint. Click to download.

- [GUnpublishedWorksQiYHXXXXXXXXXXNatureCommunicationsFinalVersionbeforeSubmissionSupplementaryInformation.docx](#)
- [GUnpublishedWorksQiYHXXXXXXXXXXNatureCommunicationsFinalVersionbeforeSubmissionSupplementaryInformation.docx](#)
- [Scheme1.png](#)
- [Scheme1.png](#)